Mapping Mantle Transition Zone Discontinuities Beneath the Central Pacific With Array Processing of SS Precursors

Chunquan Yu, Elizabeth A. Day, Maarten V. de Hoop, Michel Campillo, Robert D. van Der Hilst

AGU PUBLICATIONS

JGR

Journal of Geophysical Research: Solid Earth

RESEARCH ARTICLE
10.1002/2017JB014327

Key Points:
- Curvelet-based array processing improves the signal of *SS* precursors and the imaging of MTZ structures
- A mean MTZ thickness (239 ± 2 km) suggests an adiabatic mantle temperature of ~1,400°C beneath the Central Pacific
- Small perturbations in the depth to MTZ discontinuities argue against large-scale thermal anomalies exceeding 200 K

Supporting Information:
- Supporting Information S1

Correspondence to:
C. Yu,
yucq@gps.caltech.edu

Citation:
Yu, C., Day, E. A., de Hoop, M. V., Campillo, M., & van der Hilst, R. D. (2017). Mapping mantle transition zone discontinuities beneath the Central Pacific with array processing of *SS* precursors. *Journal of Geophysical Research: Solid Earth*, *122*, 10,364–10,378. https://doi.org/10.1002/2017JB014327

Received 13 APR 2017
Accepted 24 NOV 2017
Accepted article online 30 NOV 2017
Published online 26 DEC 2017

Mapping Mantle Transition Zone Discontinuities Beneath the Central Pacific With Array Processing of *SS* Precursors

Chunquan Yu[1,2], Elizabeth A. Day[1,3], Maarten V. de Hoop[4], Michel Campillo[1,5], and Robert D. van der Hilst[1]

[1]Department of Earth, Atmospheric and Planetary Sciences, Massachusetts Institute of Technology, Cambridge, MA, USA, [2]Now at Seismological Laboratory, California Institute of Technology, Pasadena, CA, USA, [3]Department of Earth Science and Engineering, Imperial College, London, UK, [4]Department of Computational and Applied Mathematics, Rice University, Houston, TX, USA, [5]Institut des Sciences de la Terre, Université Joseph Fourier, Grenoble, France

Abstract We image mantle transition zone (MTZ) discontinuities beneath the Central Pacific using ~120,000 broadband *SS* waveforms. With a wave packet-based array processing technique (curvelet transform), we improve the signal-to-noise ratio of *SS* precursors and remove interfering phases, so that precursors can be identified and measured over a larger distance range. Removal of interfering phases reveals possible phase shifts in the underside reflection at the *660*, that is, $S^{660}S$, which if ignored could lead to biased discontinuity depth estimates. The combination of data quantity and improved quality allows improved imaging and uncertainty estimation. Time to depth conversions after corrections for bathymetry, crustal thickness, and tomographically inferred mantle heterogeneity show that the mean depths of *410* and *660* beneath the Central Pacific are 420 ± 3 km and 659 ± 4 km, respectively. The mean MTZ thickness (239 ± 2 km) is close to global estimates and suggests an adiabatic mantle temperature of ~1,400°C for the Central Pacific. Depth variations of the *410* and *660* appear to be relatively small, with peak-to-peak amplitudes of the order of 10–15 km. The *410* and *660* are weakly anticorrelated, and MTZ is thinner beneath Hawaii and to the north and east of the hotspot and thicker southwest of it. The relatively small discontinuity topography argues against the presence of large-scale (more than 5° wide) thermal anomalies with excess temperatures over 200 K across the transition zone. The data used cannot exclude stronger thermal anomalies that are of more limited lateral extent or that are not continuous across the MTZ.

1. Introduction

The mantle transition zone (MTZ), bounded by discontinuities near 410 km and 660 km depth (hereinafter referred to as *410* and *660*; e.g., Deuss, 2009; Helffrich, 2000; Shearer, 2000), plays a critical role in mantle dynamics. The presence of the *410* and *660* is generally explained by mineralogical phase transitions from olivine to wadsleyite and from ringwoodite to perovskite + ferropericlase (Ita & Stixrude, 1992; Ringwood, 1975), respectively. With knowledge of the Clapeyron slopes of these two phase transitions, which have opposite signs (positive for *410*, negative for *660*; e.g., Bina & Helffrich, 1994; Stixrude & Lithgow-Bertelloni, 2011), lateral variations in depth to the *410* and *660* can be used to infer thermal anomalies in the mantle. For example, downward deflection of the *660* beneath the western Pacific subduction zones has been explained by the interaction of cold slabs with the surrounding hotter mantle (Shearer & Masters, 1992; Van der Hilst et al., 1993). The width of the MTZ, that is, the depth difference between *410* and *660*, can be determined more robustly (because the effect of structure above *410* is suppressed upon subtraction), but using this as a proxy for temperature requires making assumptions about the vertical extent of the anomalies.

One of the most useful data sets for mapping MTZ discontinuities is that of *SS* precursors (e.g., Shearer, 1991). *SS* precursors are underside shear wave reflections off mantle discontinuities and arrive before the main *SS* phase (the free-surface reflection). Discontinuity depth can be obtained upon time-to-depth conversion under the assumption of a velocity model. *SS* precursors provide unique opportunities to study regions far away from seismic sources and receivers, such as the Central Pacific.

The Pacific around Hawaii, where a hotspot has created a chain of volcanoes, has been central in the decades-old debate about the existence and depth of origin of mantle plumes (e.g., Morgan, 1971). The area is densely sampled by *SS* data (Figure 1), and inferences about MTZ structure here have been made from both global (e.g., Deuss, 2009; Flanagan & Shearer, 1998; Gu et al., 1998; Houser et al., 2008; Lawrence

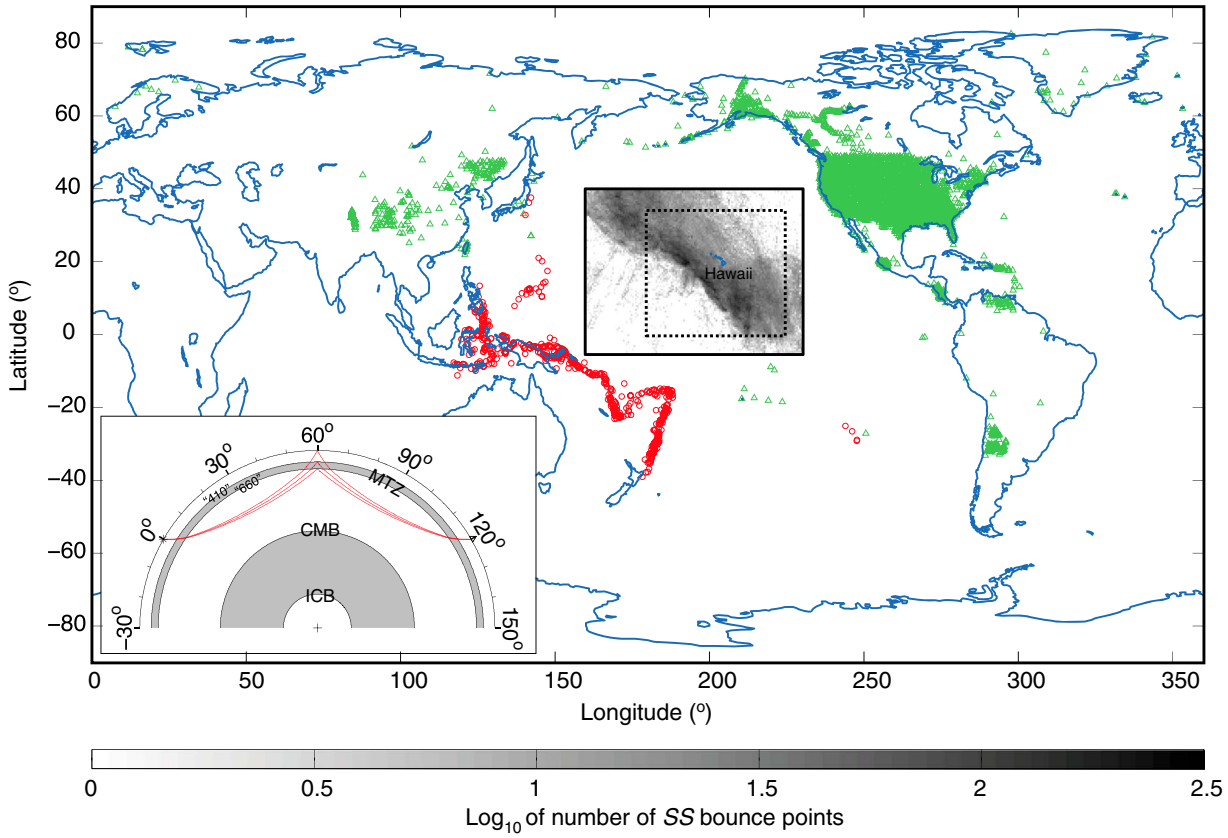

Figure 1. Map showing the study region (black box) and distribution of sources (red circles) and receivers (green triangles) used in this study. The dotted box marks the region where depths of *410* and *660* are estimated. Gray tones represent *SS* reflection point density in 0.5° by 0.5° grid sizes for data with epicentral distance 70°–170°, event magnitude (m_b) larger than 5.5, and event depth less than 75 km. Inserted schematic diagram depicts ray paths of *SS*, $S^{410}S$, and $S^{660}S$ for a source–receiver distance of 120°.

& Shearer, 2008) and regional (e.g., Cao et al., 2011; Schmerr & Garnero, 2006; Zheng et al., 2015) analyses. Nevertheless, there is little consensus on the topography of *410* and *660* and MTZ thickness in this region. In large part, this is due to the distribution of the data. While the region is sampled by many *SS*, the fact that much of the data are recorded at relatively small source–receiver distances ($\Delta < 110°$) poses several challenges. First, at these distances, the *SS* wavefield is contaminated by near-source or near-receiver multiples, risking phase misidentification and making precursor identification and measurement difficult without careful processing. Second, the sensitivity of precursor arrival times to variations in discontinuity depth decreases with decreasing source–receiver distance and increasing reflector depth, so that short distance has poorer resolution of reflector depth than large offset data, in particular for *660*. Third, as we will show, at $\Delta < 110°$, $S^{660}S$ waveforms are distorted by phase shifts upon reflection, and ignoring this effect can lead to biased depth estimates. Finally, the large-offset data that are best used for topography studies sample the region unevenly. Combined, these issues render imaging results sensitive to data selection and call for careful processing, including separation of wavefields containing precursors and interfering phases.

In this study, we use a curvelet decomposition to separate interfering phases from and suppress noise in the *SS* wavefield and estimate variations in *410* and *660* depths and MTZ thickness across a large area in the Central Pacific from time- and depth-domain common midpoint stacking of broadband *SS* waveforms. The effective suppression of interfering phases allows the use of $S^{410}S$ and $S^{660}S$ data from smaller distances than previously possible, but in contrast to a study with a similar objective (Zheng et al., 2015), we only use data beyond the range where phase shifts can occur. The phase-shifted near-offset $S^{660}S$ data, which are relatively insensitive to topography, are discarded here but can be used to estimate elasticity contrasts across the *660*.

2. Preliminary Data Analysis

2.1. Data Selection and Preprocessing

Precursors to *SS* result from underside reflections at elasticity contrasts (roughly) beneath the midpoint of the earthquake source and the receiver (Figure 1). To study the MTZ beneath the Central Pacific, we collect broadband data from the USArray Transportable Array and other regional and global networks for *SS* bounce points in the area defined by 5°S–40°N and 160°–230°E (Figure 1). We consider events (occurring between 2000 and 2014) with magnitude larger than 5.5 (to ensure sufficient signal-to-noise ratio) and focal depth less than 75 km (to minimize interference of depth phases). A minimum source–receiver distance (Δ) of 110° is often used (e.g., Deuss, 2009; Flanagan & Shearer, 1998) to avoid interference by phases such as multiples of *S*, *ScS*, and *S* diffractions (S_{diff}). For the area under study, however, such a cutoff removes much of the available data from further analysis, which may explain the lack of consistent results. Zheng et al. (2015) suppressed said multiples using a slant stack approach; here we separate the wavefields containing precursors and interfering phases and enhancing signal-to-noise of *SS* precursors with array processing based on wave packets.

The initial preprocessing steps are similar to previous *SS* precursor studies (e.g., Schmerr & Garnero, 2006). We first rotate seismograms from north and east components into radial and transverse components. The transverse (or *SH*) component seismograms are then filtered (two-pass Butterworth filter) with a passband of 0.02–0.05 Hz. We visually check all seismograms using the Crazyseismic software (Yu et al., 2017), and traces with no clear *SS* phases or low SNR (<2) are removed. Here SNR is defined as the ratio between maximum amplitude of the seismic trace in the main *SS* window ($[T_{SS} - 50 T_{SS} + 50]$ s) and that in the precursor window ($[T_{S660S} - 30 T_{S410S} + 30]$ s). Seismic traces are aligned on the first major peak of the *SS* phase (set to 0 s and unit amplitude). Polarities are reversed if necessary. Approximately 1,050 events pass these selection criteria.

Subsequently, events ($N \sim 670$) with more than 50 recordings are subjected to array processing (see section 3). The total number of selected traces is ~180,000 (of which about two thirds are used for time and depth migration in sections 4.3 and 4.4), which is more than that of previous *SS* precursor studies in the same study region (e.g., Schmerr & Garnero, 2006; Zheng et al., 2015). Controlled by the distribution of sources and receivers, most of the *SS* bounce points are located along a northwest-southeast corridor, and the Hawaiian hotspot is relatively well sampled (Figure 1).

2.2. Stacked *SS* Waveforms: Wavefield Interference

Figure 2a shows a record section of all data, stacked in 0.5° distance bins, from 70° to 170°. The stacks are aligned on the surface reflections, *SS*, whose amplitudes are normalized to unity. The major seismic phases match (reduced) travel times predicted from 1-D reference model *ak135* (Kennett et al., 1995; Figure 2b). At large distances, the stacks become increasingly noisy due to decreasing data volumes, but the *410* and *660* reflections are visible up to 160° as coherent signals at 140–170 s ($S^{410}S$) and 200–250 s ($S^{660}S$) before *SS*, respectively. While visible, at distances less than 110°, the precursors ($S^{410}S$, $S^{660}S$) are contaminated by interfering phases (in particular, multiples of *S*, *ScS*, and S_{diff}), and their arrival times cannot be reliably picked. Although less severe, phase interference and noise also affect $S^{410}S$ and $S^{660}S$ arrivals in the "clean" window. Near 120°, for example, $S^{410}S$ is distorted by a phase with slowness close to the abovementioned multiples, leading to undulations and jumps in arrival time in unprocessed data (Figure 2a).

3. Array Analysis of *SS* Precursors

3.1. Curvelet Transform and Its Application in Signal Enhancement

To improve the measurement of $S^{410}S$ and $S^{660}S$ and, thus, the imaging of MTZ discontinuities, we suppress effects of interfering phases and random noise by combined compression and denoising using a curvelet-based array processing technique. We note that, for a similar purpose, Zheng et al. (2015) used a slant stack transform, which is also localized in the space–time domain but which requires definition of a specific spatial window. Although the theoretical framework for these two methods are different, if implemented properly, both are effective in extracting weak but coherent *SS* precursors.

Curvelets (or directional wave packets) can be thought of as localized "fat" plane waves. They form a tight frame, enabling the introduction of a forward and inverse transform (Candes et al., 2006; Candes & Donoho, 2000; Smith, 1998). For fast computation, we do not use a full 3-D transform (e.g., Duchkov et al.,

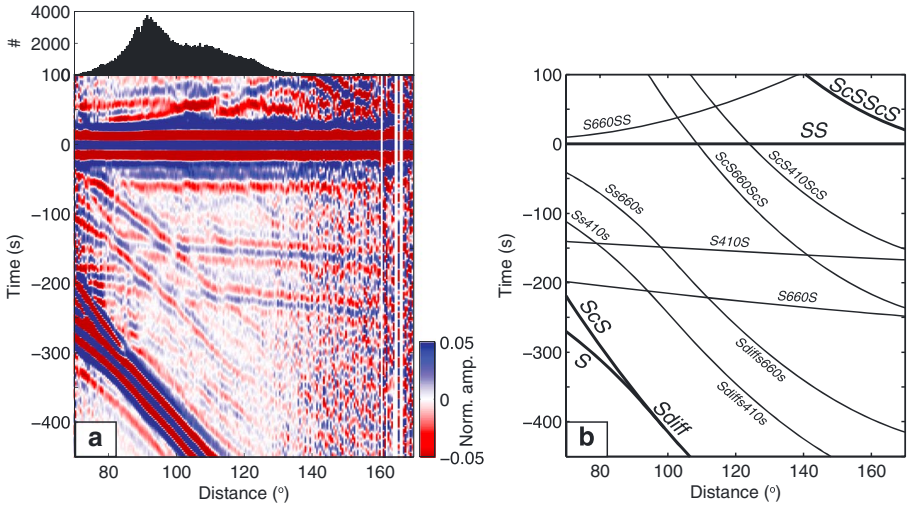

Figure 2. (a) Time–distance record section of data for all sources between 70° and 170° stacked at 0.5° intervals. The stacks are aligned on the surface reflection *SS* (set to 0 s and unit amplitude). In Figure 2a, the panel at the top shows the data distribution (number of records at each distance interval). (b) Travel times relative to *SS* predicted from *ak135* (Kennett et al., 1995).

2010) but follow a 2.5-D simplification using the rotational symmetry of the background model. Suppression of coefficients in the curvelet domain then amounts to a localized analogue of directional filtering. Phases that have different slownesses (for instance, *SS* precursors versus multiples of *S*, *ScS*, and S_{diff}) can thus be separated from one another by partitioning in the curvelet domain. The notion of scale in the curvelets is, here, correlated with the frequency content of the data. Localization, scale, and direction facilitate sparse representations of wavefields and make curvelets superior to the conventional Radon transform (or slant stacking). Numerical implementations of the curvelet transform are available at http://www.curvelet.org.

Figure 3 shows the basic principle of curvelet filtering. Two sample curvelets with same characteristic (spectral) scale overlap with each other in the space–time domain (left column). In the curvelet domain, they

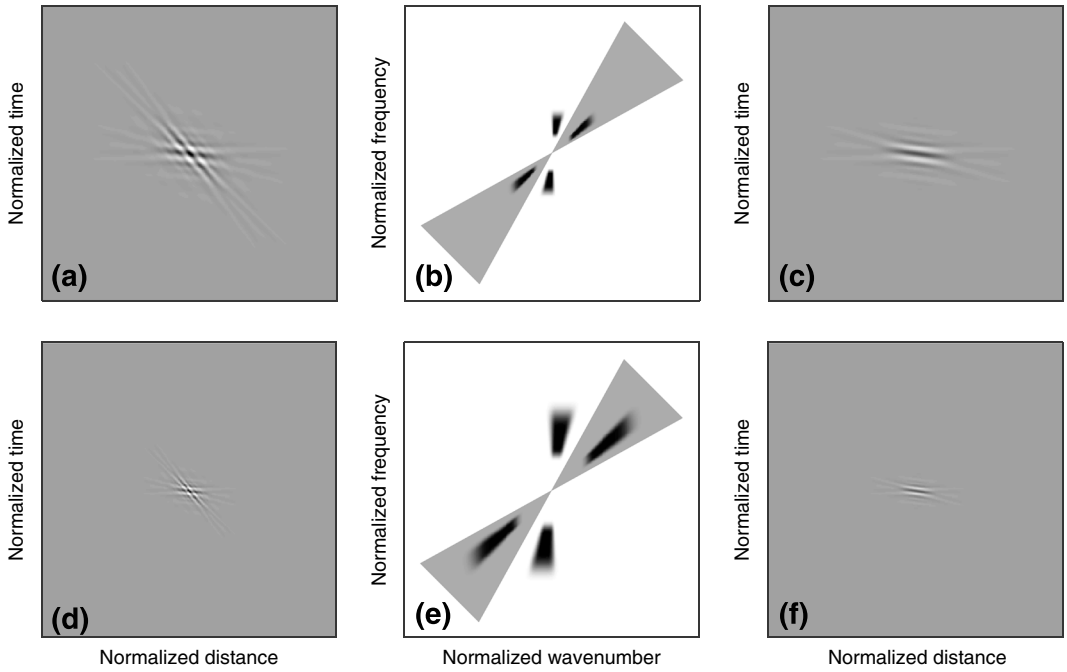

Figure 3. Illustration of curvelet filtering. (a, d) Localized plane waves (interfering) in the space–time domain. (b, e) Associated curvelet coefficients (separated) in the wavenumber–frequency domain, with (0, 0) in the center of the plot. (c, f) Filtered image after muting the coefficients in the shaded regions in Figures 3b and 3e and transformation back to the space–time domain. Figures 3d–3f are similar to Figures 3a–3c except for a finer scale.

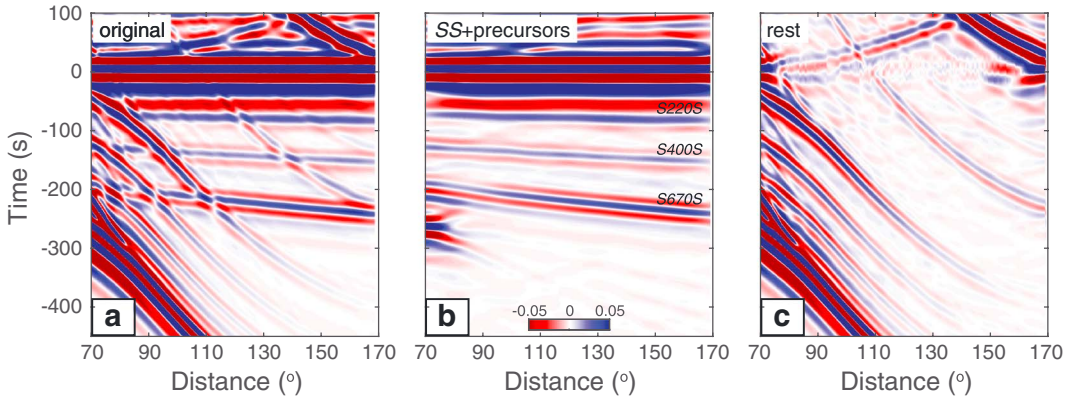

Figure 4. Synthetic tests of wavefield separation using curvelet transform. (a–c) Images of original, filtered, and residual (or signal-generated noise) of *SS* waveforms, respectively. Synthetic waveforms are computed with the reflectivity method (Fuchs & Müller, 1971) using the PREM model (Dziewonski & Anderson, 1981). Note, due to the sudden cutoff of data in the spatial domain, artifacts can exist in the filtered image near both ends of the profile, but they do not contaminate the phases of interest.

are well separated in direction, and each occupies symmetric wedges (middle column). After muting coefficients corresponding to one of the curvelets, the other is fully recovered upon inverse curvelet transformation (right column).

3.2. Tests With Synthetic Waveforms

We demonstrate the effectiveness of curvelet-based array processing with synthetic waveforms calculated (with the reflectivity method; Fuchs & Müller, 1971) for the 1-D PREM model (Dziewonski & Anderson, 1981). We note that these PREM synthetics are only used for illustration purposes and that travel time residuals used for imaging are all with respect to the *ak135* model (Kennett et al., 1995). Similar to the observed waveforms, the synthetics are filtered with a two-pass Butterworth filter with a passband of 0.02–0.05 Hz. In the synthetic waveforms (Figure 4a), precursors from the 400 km and 670 km discontinuities in PREM can be easily identified for $\Delta > 110°$. At shorter distances, however, the precursor signal is strongly contaminated by multiples of *S*, *ScS*, and S_{diff}. Note that precursors and multiples are also visible from the 220 km discontinuity in PREM.

To suppress interfering phases, we transform the synthetic waveforms from the space–time domain to the curvelet domain, mute curvelet coefficients corresponding to phases with slownesses different from *SS* precursors (with a directional taper), and transform the remainder back to the space–time domain. This curvelet decomposition effectively separates precursor signal (Figure 4b) from the interfering phases (Figure 4c). The cutoff of seismic data at either end of the distance range can generate artifacts (Figure 4b), but these edge effects are generally weak and do not degrade stacks in the time–distance range of interest.

3.3. Validation With Field Data

We further validate our array processing procedure with observed waveforms. For the purpose at hand, we select two individual earthquakes in the same source region, that is, Sumbawa, Indonesia (Table 1), but with different magnitude and, hence, noise level in the associated data. For the first, larger, event, *SS* precursors from *410* and *660* are visible in the original stack although they are contaminated by interfering phases (Figure 5a). For the second, *SS* precursors are barely visible on the original stack due to high noise level (Figure 5b).

Table 1
Two Individual Earthquakes Data in the Same Source Region

Source region	Event no.	Date[a]	Origin time (UT)	Lat. (°N)	Lon. (°E)	Depth (km)	Magnitude (M_W)
Sumbawa Region, Indonesia	1	8 November 2009	19:41:43.4	−8.21	118.63	18	6.6
	2	8 May 2010	03:22:09.7	−8.06	118.26	12	5.9

[a]Earthquake information from USGS catalog.

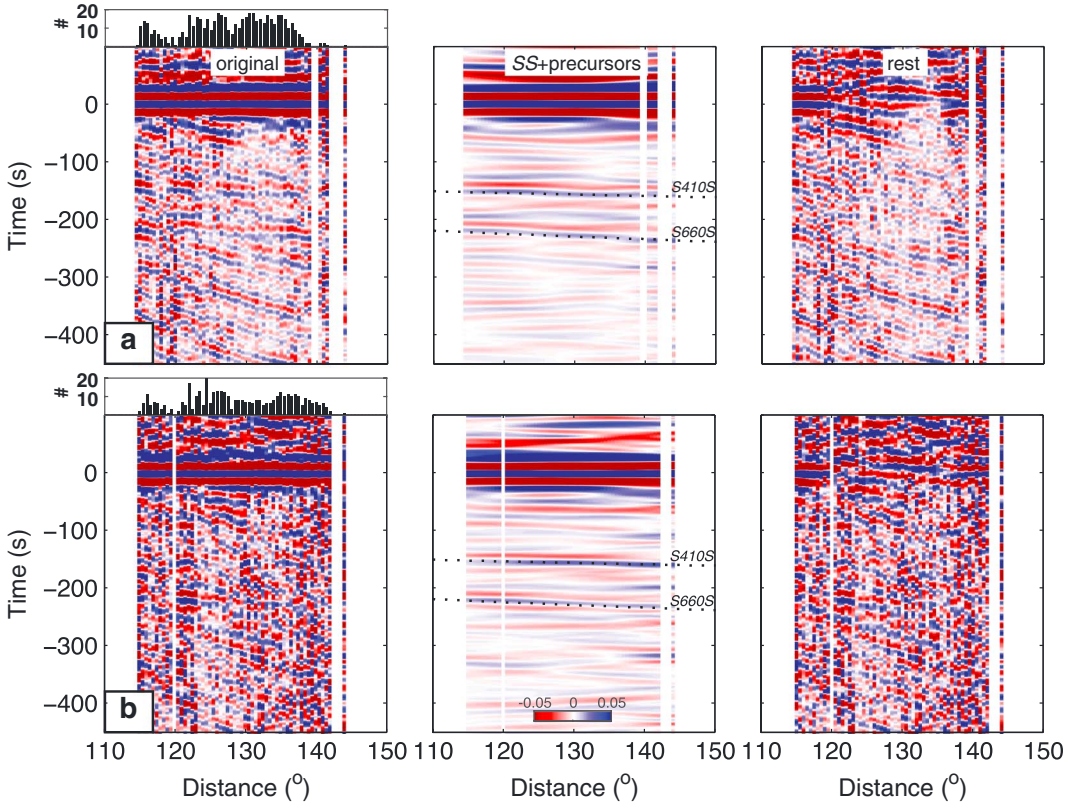

Figure 5. Field examples of noise suppression with curvelet filtering. (a, b) Data from two different earthquakes (Table 1) with different noise levels owing to the difference in source magnitude. The left, middle, and right columns show images of original, filtered, and residual of the stacked *SS* waveforms, respectively. Note both $S^{410}S$ and $S^{660}S$ are clearly visible on the filtered image and are consistent with theoretical predictions from the *ak135* model (dotted lines).

Before we transform the data from the space–time to the curvelet domain, we interpolate traces using wavefield regularization (Shang et al., 2017) to minimize artifacts generated by gaps and uneven distribution of data as a function of epicentral distance. These added traces are removed after the inverse transform and not used in subsequent analysis.

Despite phase interference and high noise levels in the original stacks (Figure 5, left panels), wavefield decomposition yield coherent $S^{410}S$ and $S^{660}S$ signal over the entire distance range (Figure 5, middle panels), with moveouts that are consistent with predictions from *ak135* (Kennett et al., 1995).

4. Results

4.1. Stacked *SS* Waveforms: Further Analysis

We apply the above procedure to all events with more than 50 reflection points in the study region. Figure 6a shows the sum of the single source stacks after combined compression and denoising using curvelets. As a result of the suppression of interfering phases, $S^{410}S$ and $S^{660}S$ stand out as coherent signals between 85° and 140°, and their arrival times and amplitudes vary smoothly with distance. At larger distances, the stacks are noisier due to sparser data coverage.

The effectiveness of curvelet filtering is demonstrated by Figure 6b, which displays the residuals after separating the wavefield containing *SS* and its precursors (Figure 6a) from the original data (Figure 2a). There is no visible coherent energy arriving at predicted arrival times of $S^{410}S$ and $S^{660}S$ (except $<80°$). Instead, interfering phases show continuous arrivals and amplitudes. We note that these multiples (Figure 6b) could, in fact, be used to image near-receiver or near-source structures with top-side reflections, for instance, beneath USArray.

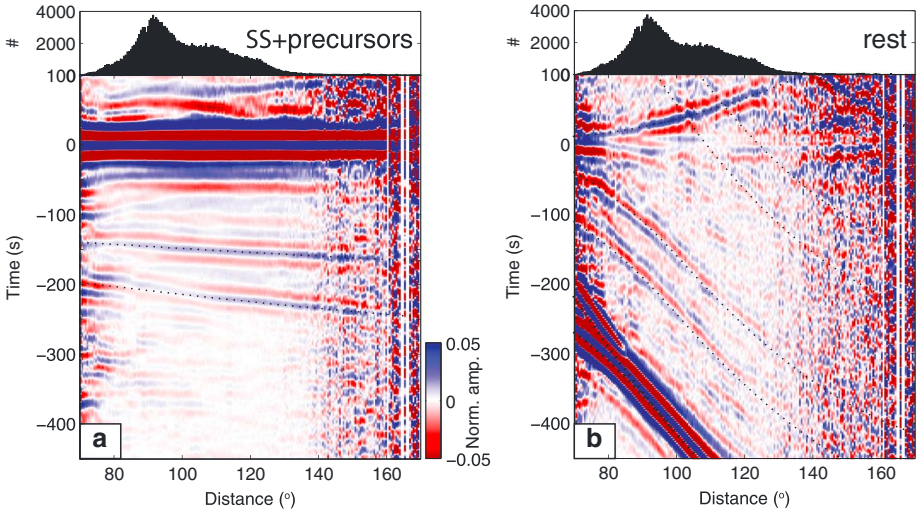

Figure 6. (a) Stacked *SS* waveforms and (b) residual after applying curvelet filtering to data for all sources in this study. Note that interfering phases, such as multiples of *S*, *ScS*, and S_{diff} and precursors of *ScSScS*, are removed. Dotted lines show predicted arrival times for *ak135* (see Figure 2b for phases).

Uncertainties of $T_{SS\text{-}S410S}$ and $T_{SS\text{-}S660S}$ over distance are greatly reduced after curvelet filtering (Figure 7). Between 95° and 140° for *410* and between 105° and 140° for *660*, $T_{SS\text{-}S410S}$ and $T_{SS\text{-}S660S}$ are consistent with predictions from *ak135* (albeit with a small, constant shift) with small perturbations over distance. Measurements from the original stack (Figure 2a), however, are more scattered (Figure 7). Even at distance between 120° and 140°, where phase interference is traditionally considered to be minimal, uncertainties in $T_{SS\text{-}S410S}$ and $T_{SS\text{-}S660S}$ are much reduced after array processing.

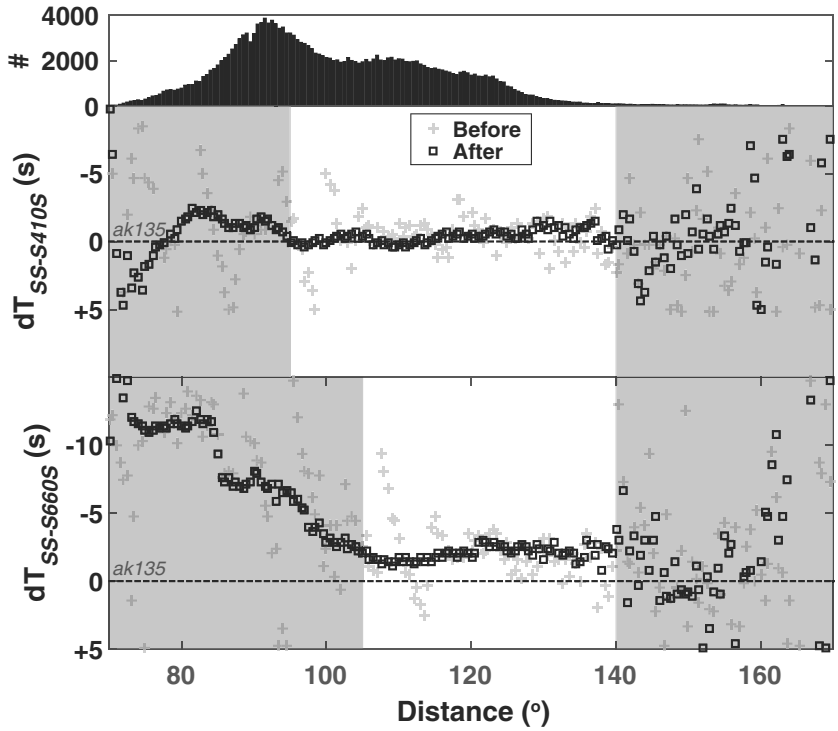

Figure 7. (middle) $T_{SS\text{-}S410S}$ and (bottom) $T_{SS\text{-}S660S}$ travel time deviations (the difference of time between observed peaks and those predicted from *ak135*) over distance. Gray pluses and black squares denote travel time deviations before and after array processing, respectively. Shaded areas mark less reliable $T_{SS\text{-}S410S}$ and $T_{SS\text{-}S660S}$ estimates. The ~12 s $T_{SS\text{-}S660S}$ moveout between 70° and 110° is mostly due to phases shifts upon reflection at the *660* (see text, section 4.2).

4.2. Time–Distance Moveout of $S^{660}S$

The moveout of $S^{410}S$ generally agrees with predictions from *ak135* (Figures 6a and 7), suggesting that *410* depth variations are minor. The situation is more complicated for $S^{660}S$. Beyond 105°, the $S^{660}S$ moveout matches the 1-D model prediction (albeit with a small, constant shift; Figures 6a and 7). Between 90° and 105°, however, the $S^{660}S$ becomes weak (and sometimes absent), and at even smaller distances, the reflections appear to move closer to *SS* (up to ~12 s). This is not an artifact of data processing as it is also discernable (between multiples) in the original stack (Figure 2a).

The apparent moveout of $S^{660}S$ at distances less than ~105° could have several origins. First, following Zheng et al. (2015), it might be tempting to attribute it to topography, with the reduced separation of *SS* and $S^{660}S$ resulting from uplift of the *660*. The problem with this explanation is that large-offset data indicate normal depths ($\delta T_{SS\text{-}S660S} \approx 0$). Topography could then only explain the observations if large offset data systematically sample other regions than small offset data. Such a systematic pattern is not observed, however, and the lateral variation in $T_{SS\text{-}S660S}$ across the region is small (section 4.3). Moreover, at short offsets, $\delta T_{SS\text{-}S660S}$ is less sensitive to changes in discontinuity depth than at large offsets due to differences in incidence angle (which increases with decreasing distance and increasing discontinuity depth): indeed, topography seen by large offset data could perhaps be missed at small offsets, but not the other way around (as would need to be the case here). Second, moveouts could be due to mantle heterogeneity not accounted for in the 1-D model used to predict arrival times. Exploring a range of moveout velocities, we find that explaining the moveout of $S^{660}S$ requires a $d\ln V_S$ of about −5% over a region of ~28° in width and ~300 km in thickness (Figure 8). Such a strong and large anomaly is not detected tomographically (e.g., French & Romanowicz, 2014; Panning et al., 2010; Ritsema et al., 2011; Simmons et al., 2010), would require unrealistic thermal or compositional anomalies, and is inconsistent with the observed $T_{SS\text{-}S410S}$ (Figure 8b). We thus rule out topography and heterogeneity as primary causes of the observed moveout.

Calculation of the $S^{660}S$ reflection coefficient, R_{S660S}, as a function of distance predicts changes in amplitude and a 180° phase shift due to change in sign of R_{S660S} (Aki & Richards, 2002). The ~12 s apparent deviation in $T_{SS\text{-}S660S}$ at short distance is close to the half period of $S^{660}S$ (~14 s) and, thus, consistent with a polarity reversal. If the effect of polarity reversal is unrecognized or ignored, then the apparent moveout of $S^{660}S$ can cause significant bias in estimated depth of *660*. The distance where the polarity flips is not always easy to measure and may vary laterally. It can be used to estimate elasticity contrasts across the *660* as well as mantle composition, but for the estimation of discontinuity depth—the objective of this study—we chose to avoid this complexity by restricting the distance range for $S^{660}S$ to larger than 105°. Since there is no polarity reversal of $S^{410}S$ in the distance range of interest, we extend the lower limit to 95° for *410*.

4.3. Lateral Variation in Differential Travel Times Between *SS* and Its Precursors

To get an idea of how MTZ discontinuities vary laterally, we probe our study region on a 5°-by-5° grid and stack traces in the time domain within 10° radius (bin) of each grid point using the conventional common midpoint stacking method (e.g., Flanagan & Shearer, 1998). The selection of grid and bin sizes is guided by the Fresnel zones of *SS* precursors. The first Fresnel zone width for *SS* precursors with a dominant period of ~30 s is about 10° (Deuss, 2009), and smaller structures are likely to be smoothed.

At each grid point, the processing steps are similar to those in section 3.3. Because the maximum distance range of data for each event is 40° (four times the bin radius at the midpoint), we extrapolate the wavefield using the event template (that is, the stack of all traces for the event as a function of distance) to minimize processing artifacts. After array processing, we obtain two single stacks for each grid point by summing results from all events and all distances (after moveout corrections to a reference distance of 130° using *ak135*) for *410* and *660*, respectively. $T_{SS\text{-}S410S}$ (or $T_{SS\text{-}S660S}$) are picked by finding the maximum cross correlation coefficients between stacked $S^{410}S$ (or $S^{660}S$) and the reference *SS* phase. Uncertainties are estimated through bootstrapping (Efron & Tibshirani, 1994): we randomly resample the data space 100 times while keeping the same number of traces.

Figure 9a shows lateral variations in $T_{SS\text{-}S410S}$, $T_{SS\text{-}S660S}$, and $T_{S410S\text{-}S660S}$. For visualization purposes, results are interpolated on a 1° × 1° grid. The mean values are reduced by corresponding predictions from the *ak135*

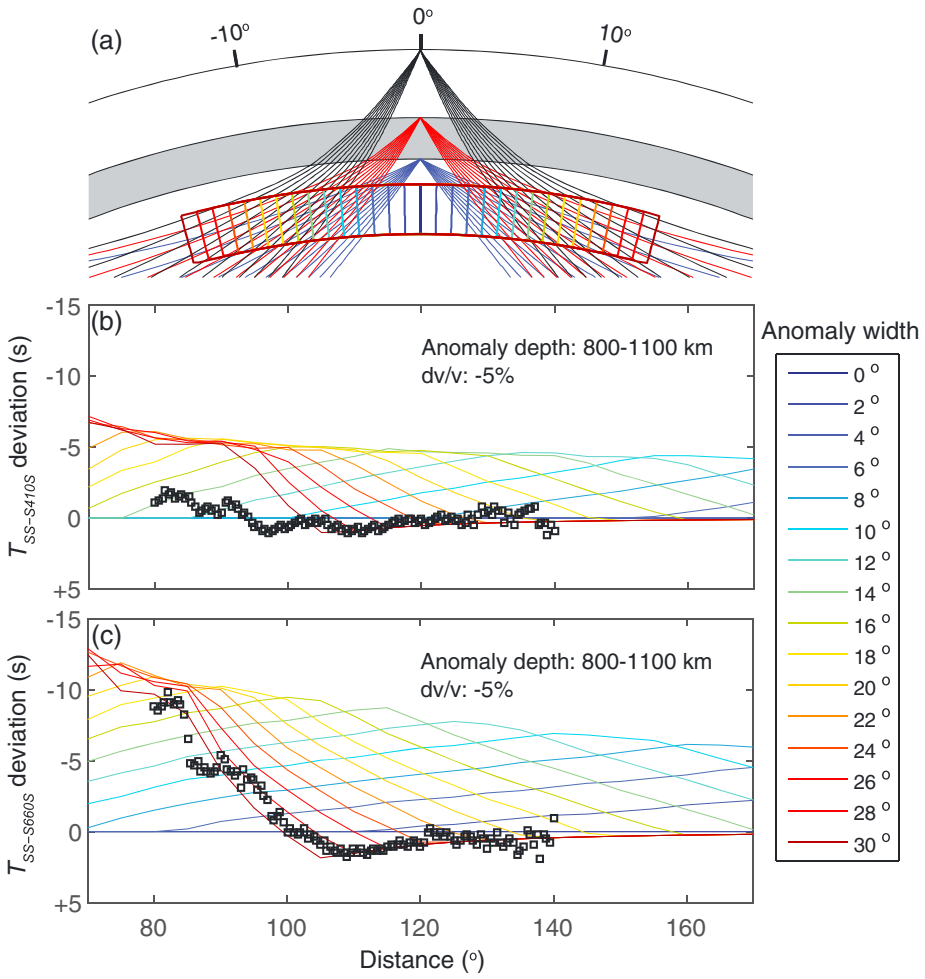

Figure 8. Estimation of T_{SS-SdS} travel time deviations due to a hypothetical velocity anomaly. (a) Ray geometry of *SS*, $S^{410}S$, and $S^{660}S$ for different source–receiver distances. The color-coded boxes show the spatial extent of hypothetical velocity anomalies used to calculate time–distance moveouts. (b) Predicted $T_{SS-S410S}$ travel time deviations for varying-width velocity anomalies. Black squares are observed $T_{SS-S410S}$ travel time deviations between 80° and 140° (same as in Figure 7). The mean value is shifted to match the theoretical prediction at $\Delta > 110°$. (c) Same as Figure 8b but for *660*. To match the observed $T_{SS-S660S}$ travel time deviations, the required anomaly must be about 28° in width, 300 km in depth, and have a 5% reduction in shear wave speed.

model. Lateral variations in $T_{SS-S410S}$ and $T_{SS-S660S}$ are within ±2 s, already suggesting that the topography on *410* and *660* is quite small. We note that $T_{SS-S410S}$ and $T_{SS-S660S}$ are stable over various stacking distance ranges after array processing (supporting information Figure S1). The spatial patterns of $T_{SS-S410S}$ and $T_{SS-S660S}$ are weakly anticorrelated ($R = -0.50$). Smaller $T_{SS-S410S}$ and larger $T_{SS-S660S}$ (hence larger $T_{S410S-S660S}$) are mainly located to the southwest of the Hawaiian hotspot. However, this region also shows relatively large uncertainties (Figure 9b). In contrast, larger $T_{SS-S410S}$ and smaller $T_{SS-S660S}$ (and, thus, smaller $T_{S410S-S660S}$) are found to the north and east of the Hawaiian. The differences in uncertainties are mainly due to the difference in data coverage (cf. Figures 1 and 9b). The uncertainties in $T_{SS-S410S}$ are generally smaller than in $T_{SS-S660S}$.

4.4. Depths to *410* and *660* and MTZ Thickness

To determine the depth to *410* and *660* from $T_{SS-S410S}$ and $T_{SS-S660S}$, respectively, it is necessary to migrate traces from time to depth. We use 1-D layered Earth models to trace seismic rays and apply corrections for bathymetry (Amante & Eakins, 2009), crustal thickness (Laske et al., 2013), and tomographically inferred 3-D mantle heterogeneity. Traces are migrated to depth after array processing and stacked using the common midpoint stacking method.

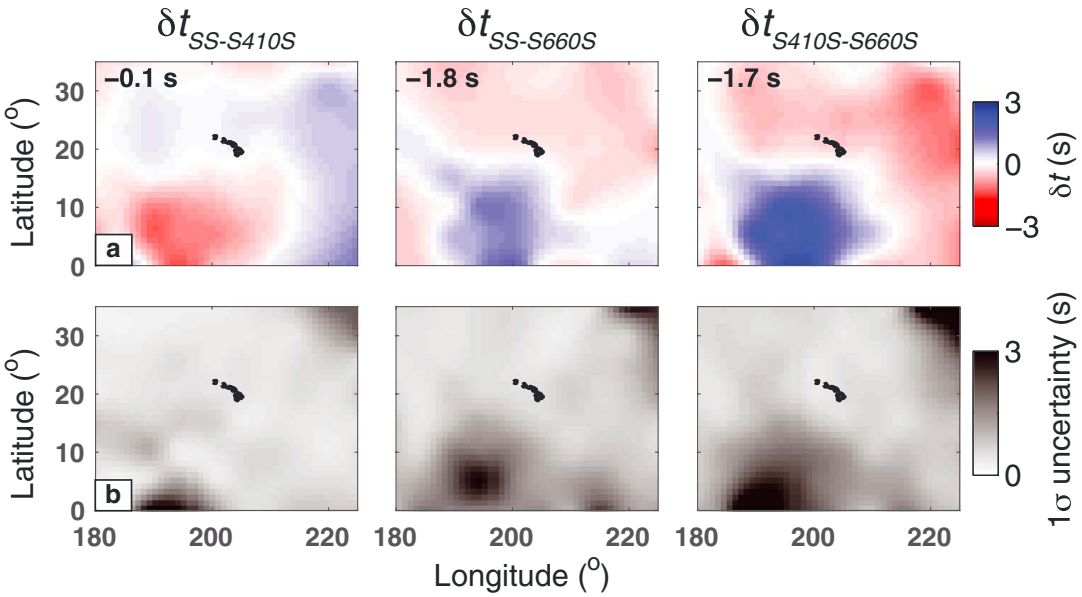

Figure 9. (a) Map of travel time perturbations of (left) $T_{SS\text{-}S410S}$, (middle) $T_{SS\text{-}S660S}$, and (right) $T_{S410S\text{-}S660S}$ relative to those calculated from the *ak135* model. Mean values are shown at the upper left corner of each plot. (b) 1-sigma uncertainties of above estimates based on bootstrap analysis.

We compare migration results using four different global tomography models: S40RTS (Ritsema et al., 2011), SEMUCB-WM1 (French & Romanowicz, 2014), SAW642ANB (Panning et al., 2010), and GyPSuM (Simmons et al., 2010). All maps show deeper *410* beneath and to the east of the Hawaiian hotspot and shallower *410* to the southwest of it (Figure 10). For S40RTS (Ritsema et al., 2011), SEMUCB-WM1 (French & Romanowicz, 2014), and SAW642ANB (Panning et al., 2010), the *660* is deep southwest of the Hawaiian hotspot and shallow to the north of it. The deep *660* of the former two models further extends to the west of the hotspot. Corrections based on GyPSuM (Simmons et al., 2010) also yield a slightly deeper *660* west of the Hawaiian hotspot but suggests smaller (residual) *660* depth variations. Uncertainties in the depths of *410* and *660* and thickness of MTZ have similar distribution as those in Figure 9b (multiplied by a factor of ~3 upon time-to-depth conversion). The larger uncertainties southwest of the Hawaiian hotspot are also evident in reflectivity profiles across the region (Figure 11).

The mean depths of *410* and *660* are 420 ± 3 km and 659 ± 4 km, respectively. Their peak-to-peak topographies are similar: 10–15 km (Figure 10). The depth difference between *410* and *660*, or the MTZ thickness, is more robust as it is less affected by upper mantle heterogeneity. The four models show similar patterns of MTZ thickness distribution, but peak-to-peak topography for GyPSuM is smaller than for the other models used (Figure 10). The mean MTZ thickness in our study region is 239 ± 2 km, close to the global average (Deuss, 2009). The MTZ is thick southwest of the Hawaiian hotspot, whereas the MTZ is relatively thin beneath Hawaii as well as to the north and east of the hotspot (Figure 10). The correlation between the average shear wave anomaly in the MTZ and the MTZ thickness is generally low (Figure 12), with only S40RTS yielding a (weakly) positive correlation (R = 0.48).

5. Discussion

5.1. Comparison With Previous Studies

We find a thin MTZ beneath Hawaii and to the north and east of the hotspot and a thicker MTZ southwest of it. These results are in agreement with some but not all independent studies. Previous results on *410* and *660* topographies and MTZ thickness beneath the Central Pacific are highly variable, in particular for the "thin" MTZ or anomalously shallow *660* that is often used as diagnostic for high temperatures. A thin MTZ has been reported west (Gu et al., 2003), beneath (Lawrence & Shearer, 2008), and southeast (Schmerr & Garnero, 2006) of the Hawaiian hotspot, while Zheng et al. (2015) find a very shallow *660* to the east of Hawaii. Evidence for a relatively thick MTZ is more robust, with Deuss (2009), Houser et al. (2008), Cao et al. (2011), Zheng et al.

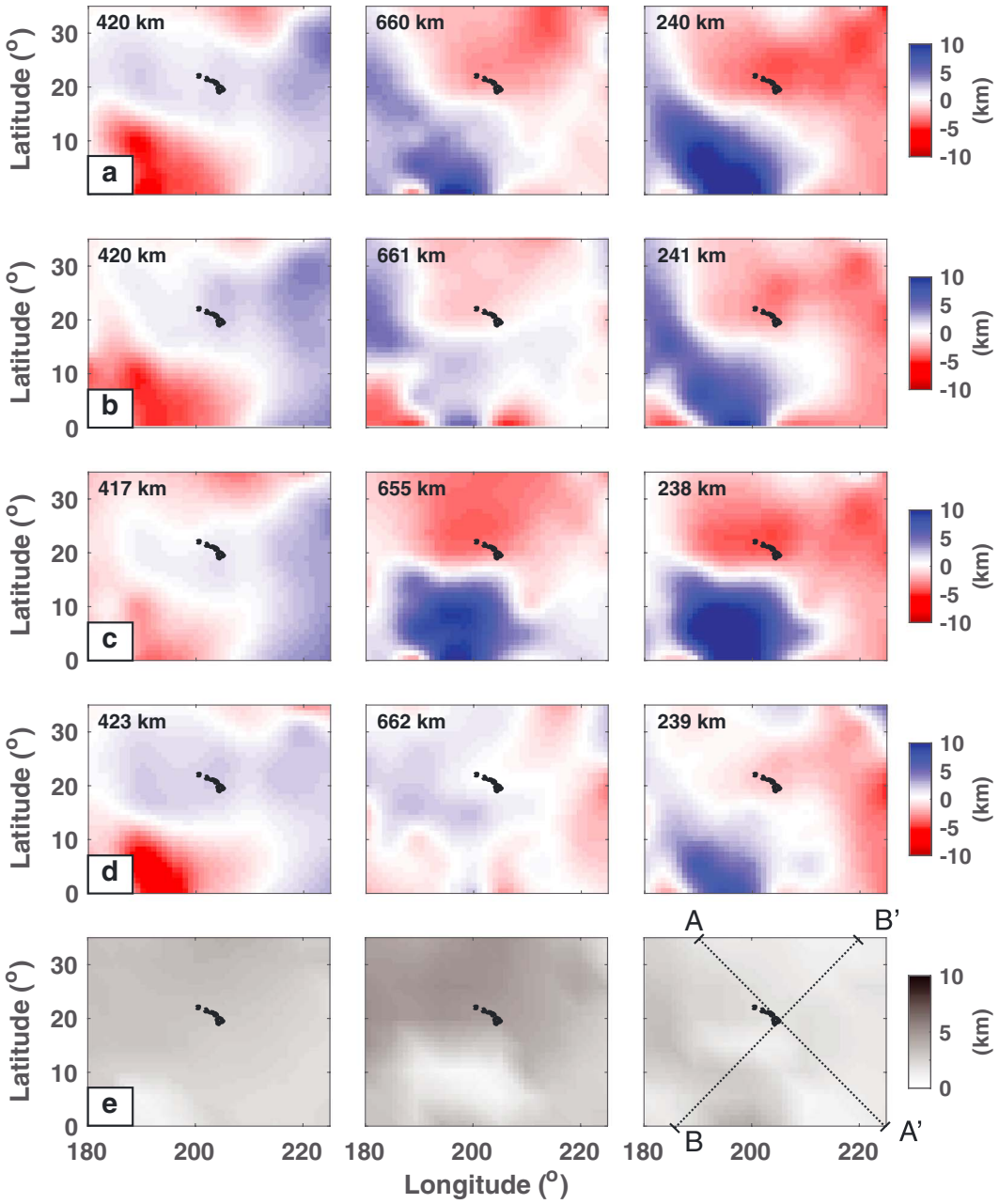

Figure 10. Map of depth estimates of (left) *410*, (middle) *660*, and (right) the mantle transition zone thickness. (a–d) Results are shown after tomographic corrections using four different tomography models: S40RTS (Ritsema et al., 2011), SEMUCB-WM1 (French & Romanowicz, 2014), SAW642ANB (Panning et al., 2010), and GyPSuM (Simmons et al., 2010), respectively. Mean values are shown at the upper left corner of each plot. (e) 1-sigma uncertainties of estimates for the above four tomography models.

(2015), and the data presented here all suggesting a deeper *660* (and, hence, thicker MTZ) west or southwest of Hawaii. Inconsistencies can result from the uneven distribution of the data and the differences in selection and processing of particular subsets of the unevenly distributed *SS* data.

As shown (e.g., Figure 6a), much of the data that sample the region are recorded at relatively small source–receiver distances ($\Delta < 110°$). Cao et al. (2011) and Zheng et al. (2015) used these short-distance data in attempts to extend the imaging of *410* and *660* topography beyond the regions that are sampled well by far-offset data ($\Delta > 110°$). This poses particular challenges, however, especially for the *660*. First, contamination by multiples increases the risk of phase misidentification. Indeed, it is likely that the anomalously deep

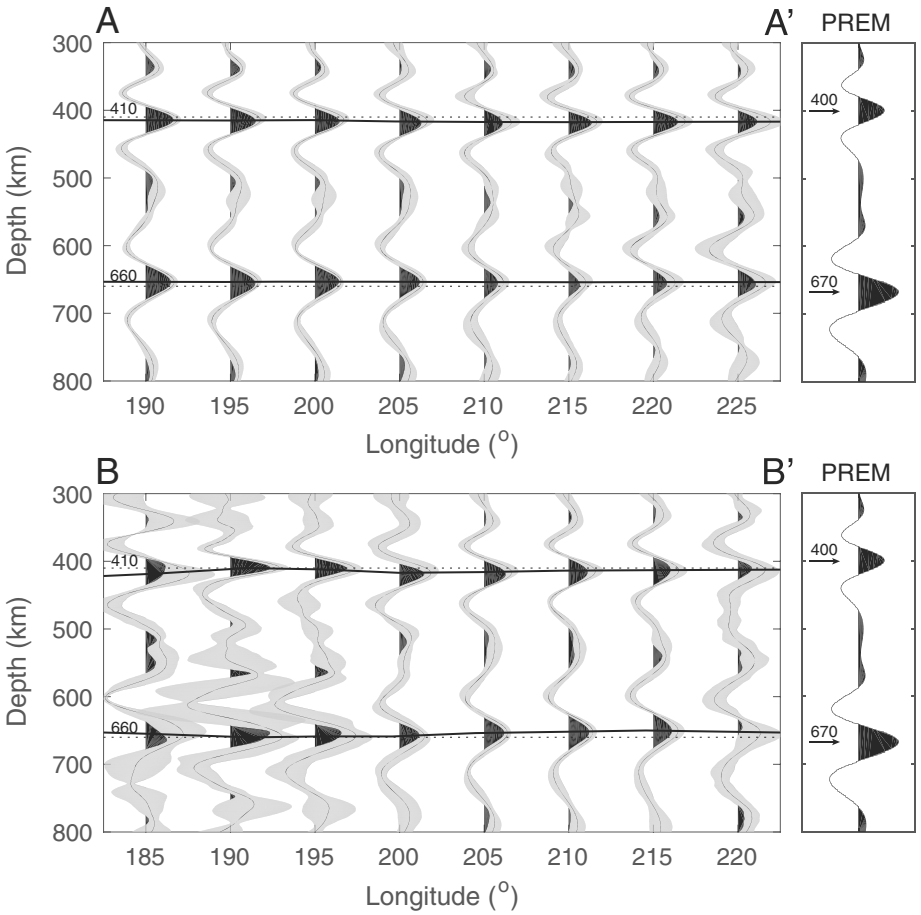

Figure 11. Two cross-sections showing migrated *SS* waveforms. The shaded regions bracketing seismic traces represent 2-sigma uncertainties. Robust positive amplitudes are filled with black colors. Thick horizontal lines trace the depths of *410* and *660*. Locations of AA′ and BB′ profiles are shown in Figure 10e. S40RTS is used for tomographic corrections. Only data with epicentral distance larger than 105° are used. For comparison, the synthetic traces at 130°, computed with the PREM model and converted to the depth domain, are shown in the right column.

660 reported by Cao et al. (2011) west of Hawaii resulted from misinterpretation of multiples of S_{diff} ($S_{diff}s_{410}s$ and $S_{diff}s_{660}s$) arriving just before $S^{660}S$ that were not adequately suppressed in the slowness stacks of the Generalized Radon Transform. Removal of the multiples (this study) still yields a deep *660* in this region, but not as deep as suggested in Cao et al. (2011). Effectively, this obviates the need to invoke a post-garnet transition to explain the deep *660*. Second, phase shifts can produce an apparent moveout toward later $S^{660}S$ arrivals (Figure 6a), which, if ignored or not recognized, can lead to substantial depth bias in regions preferentially sampled by these short-offset data. We suspect that this explains the dramatic uplift of the *660* (to 620 km depth) east of Hawaii reported by Zheng et al. (2015), who removed multiples but interpreted the late $S^{660}S$ arrivals at short distances in terms of topography alone without regard for possible phase shifts.

5.2. Moderately High Temperatures in the MTZ Beneath the Central Pacific

The *410* and *660* topographies are often attributed to lateral variations in temperature at those depths. High MTZ temperatures predict deflection of the *410* and uplift of the *660*; vice versa, low MTZ temperature predicts uplifted *410* and deflected *660* (e.g., Stixrude & Lithgow-Bertelloni, 2011). However, seismological estimation of the absolute depths of *410* and 660 can potentially have large uncertainties due to strong heterogeneities in the upper mantle. The MTZ thickness is a more robust estimate as it is mostly sensitive to the structure within the MTZ and is, therefore, more widely used than absolute depths of *410* and *660* to infer thermal anomalies (e.g., Deuss, 2009; Gu et al., 2003; Houser et al., 2008; Lawrence & Shearer, 2008; Schmerr & Garnero, 2006).

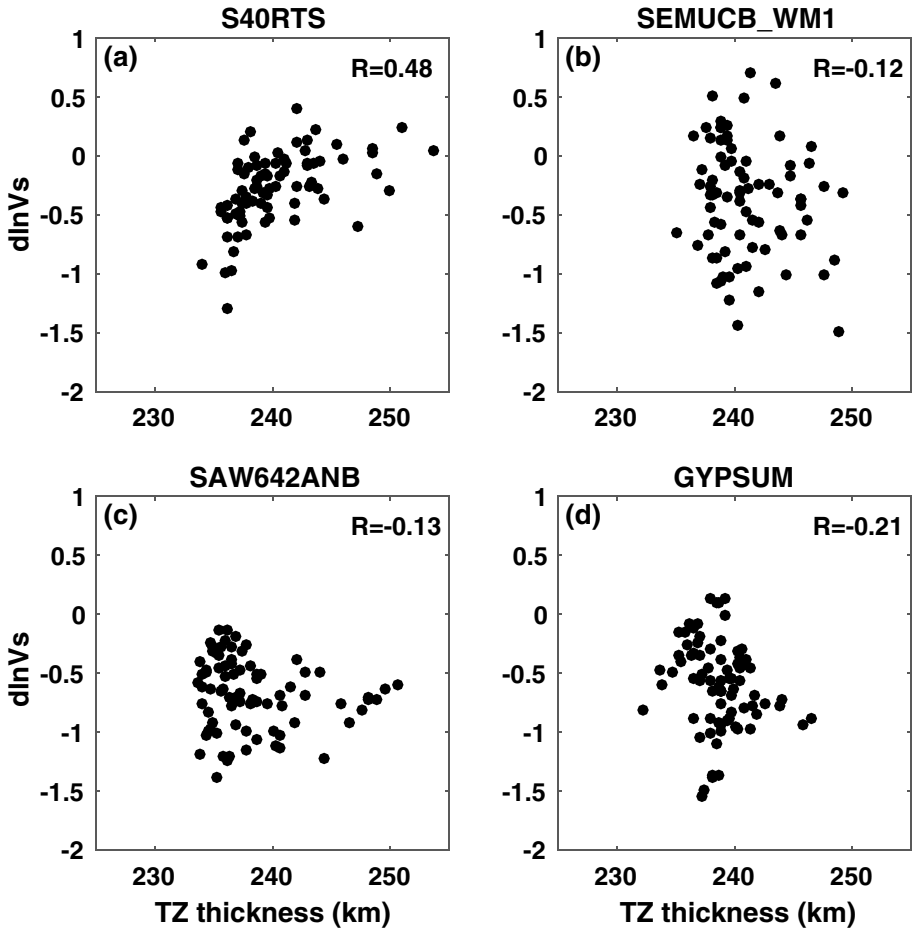

Figure 12. Plots of MTZ thickness versus average shear wave speed perturbation in the MTZ. (a–d) For S40RTS (Ritsema et al., 2011), SEMUCB-WM1 (French & Romanowicz, 2014), SAW642ANB (Panning et al., 2010), and GyPSuM (Simmons et al., 2010), respectively. Correlation coefficients (*R*) are shown at the upper right corner of each plot.

Assuming a bulk mantle composition close to pyrolitic, the ~240 km mean MTZ thickness in the Central Pacific suggests an average adiabatic mantle temperature of ~1,400°C (e.g., Stixrude & Lithgow-Bertelloni, 2011). A thin MTZ and shallow *660* suggest that the MTZ beneath, north, and east of Hawaii is slightly hotter than average. Lateral variations in MTZ thickness in the study region do not generally exceed 20 km. Clapeyron slopes of +3.0 MPa/K and −2.0 MPa/K for *410* and *660*, respectively (Bina & Helffrich, 1994), yield large-scale lateral variations in temperature in the MTZ beneath the Central Pacific of the order of 150–200 K, which would be on the low side of the 150–300 K range of excess temperatures required to explain intraplate basalt chemistry (e.g., Herzberg et al., 2007; Putirka et al., 2007; Schilling, 1991).

There are two important caveats. First, our data have limited lateral resolution due to the large Fresnel zone of *SS* precursors, and small-scale (<5°) thermal anomalies (such as presumed narrow "plumes") are beyond our detectability. Second, interpretations based on the combined use of *410* and *660* (as is the case when using MTZ thickness) rely on assumptions about the vertical extent of the thermal anomalies. Although there is generally an anticorrelation between *410* and *660*, the correlation coefficient ($R = -0.50$) is small (Figures 9 and 10). Furthermore, there is no clear evidence of positive correlation between the average shear wave speed in the MTZ and the MTZ thickness (except for a weak, positive correlation for the S40RTS model). Combined, these observations suggest either that mantle chemistry is more complicated than (the pyrolitic) olivine system invoked above or that thermal anomalies do not form continuous vertical structures.

6. Conclusions

With a curvelet-based array processing technique, we improve the signal-to-noise ratio of *SS* precursors by suppressing interfering phases and random noise. It also extends the useable data set to shorter epicentral distance than was used in earlier studies, in particular for the *410*. We detect polarity reversals of $S^{660}S$ that may potentially bias the depth estimation of *660* if they are not recognized or interpreted as such. Results from time-to-depth migration after corrections for bathymetry, crustal thickness, and 3-D mantle heterogeneities (for a range of tomography models) show that the topography of the *410* and *660* in the Central Pacific is small. Peak-to-peak amplitudes of *410* and *660* are of the order of 10–15 km. The mean MTZ thickness (~240 km) is close to the global average. Thick MTZ is mainly inferred to the southwest of the Hawaiian hotspot, but in view of the large uncertainty (mostly due to sparse data coverage), interpreting this observation demands caution. Thinner MTZ is found beneath, north, and east of the Hawaiian hotspot. If interpreted in terms of temperature alone, our results suggest that in this region lateral variation in the temperatures across the MTZ is of the order of 150–200 K, which is consistent with the geochemistry of Hawaiian basalts, but our results cannot rule out the existence of stronger thermal anomalies at smaller scales ($<5°$).

Acknowledgments

All broadband seismic waveforms were downloaded from IRIS DMC (Incorporated Research Institutions for Seismology, Data Management Center). The data set generated in this study is available upon request from the corresponding author. We thank C. Houser and an anonymous reviewer for constructive comments. M.d.H. was supported by the Simons Foundation and NSF-DMS 1559587, R.v.d.H. acknowledges a Royal Society Fellowship to support travel to Imperial College, and M.C. is a Schlumberger Visiting Professor at MIT.

References

Aki, K., & Richards, P. G. (2002). *Quantitative seismology*. Sausalito, CA: University Science Books.

Amante, C., & Eakins, B. W. (2009). ETOPO1 1 arc-minute global relief model: Procedures, data sources and analysis, NOAA Technical Memorandum NESDIS NGDC-24.

Bina, C. R., & Helffrich, G. (1994). Phase transition Clapeyron slopes and transition zone seismic discontinuity topography. *Journal of Geophysical Research*, *99*(B8), 15,853–15,860. https://doi.org/10.1029/94JB00462

Candes, E., Demanet, L., Donoho, D., & Ying, L. (2006). Fast discrete curvelet transforms. *Multiscale Modeling and Simulation*, *5*(3), 861–899. https://doi.org/10.1137/05064182X

Candes, E. J., & Donoho, D. L. (2000). Curvelets: A surprisingly effective nonadaptive representation for objects with edges, edited, DTIC Document.

Cao, Q., Van der Hilst, R., De Hoop, M., & Shim, S.-H. (2011). Seismic imaging of transition zone discontinuities suggests hot mantle west of Hawaii. *Science*, *332*(6033), 1068–1071. https://doi.org/10.1126/science.1202731

Deuss, A. (2009). Global observations of mantle discontinuities using *SS* and *PP* precursors. *Surveys in Geophysics*, *30*(4-5), 301–326. https://doi.org/10.1007/s10712-009-9078-y

Duchkov, A. A., Andersson, F., & de Hoop, M. V. (2010). Discrete almost-symmetric wave packets and multiscale geometrical representation of (seismic) waves. *IEEE Transactions on Geoscience and Remote Sensing*, *48*(9), 3408–3423. https://doi.org/10.1109/tgrs.2010.2046177

Dziewonski, A. M., & Anderson, D. L. (1981). Preliminary reference Earth model. *Physics of the Earth and Planetary Interiors*, *25*(4), 297–356. https://doi.org/10.1016/0031-9201(81)90046-7

Efron, B., & Tibshirani, R. J. (1994). *An introduction to the bootstrap*. Boca Raton, FL: CRC Press.

Flanagan, M. P., & Shearer, P. M. (1998). Global mapping of topography on transition zone velocity discontinuities by stacking *SS* precursors. *Journal of Geophysical Research*, *103*(B2), 2673–2692. https://doi.org/10.1029/97JB03212

French, S., & Romanowicz, B. (2014). Whole-mantle radially anisotropic shear velocity structure from spectral-element waveform tomography. *Geophysical Journal International*, *199*(3), 1303–1327. https://doi.org/10.1093/gji/ggu334

Fuchs, K., & Müller, G. (1971). Computation of synthetic seismograms with the reflectivity method and comparison with observations. *Geophysical Journal International*, *23*(4), 417–433. https://doi.org/10.1111/j.1365-246X.1971.tb01834.x

Gu, Y. J., Dziewonski, A. M., & Agee, C. B. (1998). Global de-correlation of the topography of transition zone discontinuities. *Earth and Planetary Science Letters*, *157*(1-2), 57–67. https://doi.org/10.1016/S0012-821X(98)00027-2

Gu, Y. J., Dziewoński, A. M., & Ekström, G. (2003). Simultaneous inversion for mantle shear velocity and topography of transition zone discontinuities. *Geophysical Journal International*, *154*(2), 559–583. https://doi.org/10.1046/j.1365-246X.2003.01967.x

Helffrich, G. (2000). Topography of the transition zone seismic discontinuities. *Reviews of Geophysics*, *38*(1), 141–158. https://doi.org/10.1029/1999RG000060

Herzberg, C., Asimow, P. D., Arndt, N., Niu, Y., Lesher, C., Fitton, J., … Saunders, A. (2007). Temperatures in ambient mantle and plumes: Constraints from basalts, picrites, and komatiites. *Geochemistry, Geophysics, Geosystems*, *8*, Q02006. https://doi.org/10.1029/2006GC001390

Houser, C., Masters, G., Flanagan, M., & Shearer, P. (2008). Determination and analysis of long-wavelength transition zone structure using *SS* precursors. *Geophysical Journal International*, *174*(1), 178–194. https://doi.org/10.1111/j.1365-246X.2008.03719.x

Ita, J., & Stixrude, L. (1992). Petrology, elasticity, and composition of the mantle transition zone. *Journal of Geophysical Research*, *97*(B5), 6849–6866. https://doi.org/10.1029/92JB00068

Kennett, B., Engdahl, E., & Buland, R. (1995). Constraints on seismic velocities in the Earth from traveltimes. *Geophysical Journal International*, *122*(1), 108–124. https://doi.org/10.1111/j.1365-246X.1995.tb03540.x

Laske, G., Masters, G., Ma, Z., & Pasyanos, M. (2013). Update on CRUST1. 0-A 1-degree global model of Earth's crust. Paper presented at EGU General Assembly Conference Abstracts.

Lawrence, J. F., & Shearer, P. M. (2008). Imaging mantle transition zone thickness with *SdS-SS* finite-frequency sensitivity kernels. *Geophysical Journal International*, *174*(1), 143–158. https://doi.org/10.1111/j.1365-246X.2007.03673.x

Morgan, W. J. (1971). Convection plumes in the lower mantle. *Nature*, *230*(5288), 42–43. https://doi.org/10.1038/230042a0

Panning, M., Lekić, V., & Romanowicz, B. (2010). Importance of crustal corrections in the development of a new global model of radial anisotropy. *Journal of Geophysical Research*, *115*, B12325. https://doi.org/10.1029/2010JB007520

Putirka, K. D., Perfit, M., Ryerson, F., & Jackson, M. G. (2007). Ambient and excess mantle temperatures, olivine thermometry, and active vs. passive upwelling. *Chemical Geology*, *241*(3-4), 177–206. https://doi.org/10.1016/j.chemgeo.2007.01.014

Ringwood, A. E. (1975). *Composition and petrology of the Earth's mantle*. New York: McGraw-Hill.

Ritsema, J., Deuss, A., Van Heijst, H., & Woodhouse, J. (2011). S40RTS: A degree-40 shear-velocity model for the mantle from new Rayleigh wave dispersion, teleseismic traveltime and normal-mode splitting function measurements. *Geophysical Journal International*, *184*(3), 1223–1236. https://doi.org/10.1111/j.1365-246X.2010.04884.x

Schilling, J.-G. (1991). Fluxes and excess temperatures of mantle plumes inferred from their interaction with migrating mid-ocean ridges. *Nature*, *352*(6334), 397–403. https://doi.org/10.1038/352397a0

Schmerr, N., & Garnero, E. (2006). Investigation of upper mantle discontinuity structure beneath the central Pacific using *SS* precursors. *Journal of Geophysical Research*, *111*, B08305. https://doi.org/10.1029/2005JB004197

Shang, X., de Hoop, M. V., & van der Hilst, R. D. (2017). Common conversion point stacking of receiver functions versus passive-source reverse time migration and wavefield regularization. *Geophysical Journal International*, *209*(2), 923–934. https://doi.org/10.1093/gji/ggx069

Shearer, P. M. (1991). Constraints on upper mantle discontinuities from observations of long-period reflected and converted phases. *Journal of Geophysical Research*, *96*(B11), 18,147–18,182. https://doi.org/10.1029/91JB01592

Shearer, P. M. (2000). Upper mantle seismic discontinuities. *Earth's deep interior: Mineral physics and tomography from the atomic to the global scale*, *115-131*.

Shearer, P. M., & Masters, T. G. (1992). Global mapping of topography on the 660-km discontinuity. *Nature*, *355*(6363), 791–796. https://doi.org/10.1038/355791a0

Simmons, N. A., Forte, A. M., Boschi, L., & Grand, S. P. (2010). GyPSuM: A joint tomographic model of mantle density and seismic wave speeds. *Journal of Geophysical Research*, *115*, B12310. https://doi.org/10.1029/2010JB007631

Smith, H. F. (1998). A parametrix construction for wave equations with $C^{1,1}$ coefficients, paper presented at Annales de l'institut Fourier.

Stixrude, L., & Lithgow-Bertelloni, C. (2011). Thermodynamics of mantle minerals-II. Phase equilibria. *Geophysical Journal International*, *184*(3), 1180–1213. https://doi.org/10.1111/j.1365-246X.2010.04890.x

Van der Hilst, R., Engdahl, E., & Spakman, W. (1993). Tomographic inversion of *P* and *pP* data for aspherical mantle structure below the northwest Pacific region. *Geophysical Journal International*, *115*(1), 264–302. https://doi.org/10.1111/j.1365-246X.1993.tb05603.x

Yu, C., Zheng, Y., & Shang, X. (2017). Crazyseismic: A MATLAB GUI-based software package for passive seismic data preprocessing. *Seismological Research Letters*, *88*(2A), 410–415. https://doi.org/10.1785/0220160207

Zheng, Z., Ventosa, S., & Romanowicz, B. (2015). High resolution upper mantle discontinuity images across the Pacific Ocean from *SS* precursors using local slant stack filters. *Geophysical Journal International*, *202*(1), 175–189. https://doi.org/10.1093/gji/ggv118